Nonlinear Phononic Slidetronics

Pooja Rani* and Dominik M. Juraschek†
Department of Applied Physics and Science Education, Eindhoven University of Technology, 5612 AP Eindhoven, Netherlands and School of Physics and Astronomy, Tel Aviv University, Tel Aviv 6997801, Israel

(Received 21 November 2025; revised 23 July 2026; accepted 23 September 2026; published 2 November 2026)

Layered van der Waals ferroelectrics are conventionally switched by sliding the different layers between stacking orders with opposing electric polarizations. Ultrashort laser pulses have been proposed to launch shear modes and induce switching, with often unfeasible large pulse energies, however. Here, we demonstrate switching of ferroelectricity in bilayer hexagonal boron nitride through nonlinearly excited phonons. We show that the efficiencies of conventional coherent phonon excitation mechanisms, including infrared absorption and Raman scattering techniques, are too low to overcome the energy barrier separating the two ferroelectric states. We demonstrate instead that excitation of high-frequency intralayer modes leads to a tilting of the interlayer potential-energy landscape that enables changing the stacking order. Our results provide an avenue toward efficient phononic slidetronics, enabling ultrafast control of the stacking order in van der Waals materials.

DOI: 10.1103/5kfl-11m1

Ultrafast control of ferroelectricity promises applications in advanced data processing devices operating on femto- and picosecond timescales. Recent advances have focused on the manipulation of the crystal structure itself through coherent and nonlinear excitation of lattice vibrations (phonons) with ultrashort laser pulses, which achieved transient switching [1–6] and inducing [7–10] of ferroelectricity. A major challenge in bulk ferroelectric materials is posed by the electric depolarizing field that prevents permanent reversal of the ferroelectric polarization in these excitation protocols [2,11,12]. Layered van der Waals ferroelectrics, in contrast, may circumvent this problem due to the reduced dimensionality of bi- and multilayer systems [13,14].

Layered van der Waals ferroelectrics can be switched by changing the stacking configuration when sliding the different layers with respect to each other, which has lead to the emergent field of sliding ferroelectricity [15–21]. From a phononic perspective, the sliding motion can be expressed in terms of low-frequency shear modes that can be launched with ultrashort laser pulses [22–25]. Recent theoretical studies have since suggested that these light-driven shear-mode dynamics could be utilized to switch the stacking order and thus ferroelectric polarization in various van der Waals materials [25–30]. A major challenge is posed by the weak light-matter couplings that make ferroelectric switching unfeasible with experimentally achievable pulse energies.

Here, we demonstrate switching of ferroelectric polarization in bilayer hexagonal boron nitride (h-BN) through nonlinearly driven phonons. Using a combination of first-principles calculations and phenomenological modeling, we show that all common mechanisms of coherent phonon excitation for large band-gap semiconductors and insulators, including infrared absorption (IRA), ionic Raman scattering (IRS) [31,32], impulsive stimulated Raman scattering (ISRS) [33], and terahertz sum-frequency excitation (THz SFE) [34,35], do not yield sufficiently large shear-mode amplitudes to overcome the energy barrier between the stacking orders. We then in contrast show how coherently excited intralayer modes tilt the interlayer potential-energy landscape and enable switching for experimentally achievable pulse energies. This involves a dynamical modification of the shear modes potential beyond conventional phononic rectification [32,36–38]. Our calculations show that nonlinear phononic slidetronics provides efficient and ultrafast control over the stacking order in van der Waals materials.

Properties of h-BN—We begin by calculating the properties of h-BN from first principles using density functional theory. We computed phonon eigenfrequencies, eigenvectors, Raman tensors, and nonlinear phonon couplings. We obtain a large band gap of 6.3 eV, consistent with previous calculations [39,40] and suitable for phonon driving using strong pulses. We find the eigenfrequency of the doubly degenerate shear mode with E symmetry to be $\Omega_s/(2\pi) = 0.94$ THz. For the full list of phonon modes and computational details, see Supplemental Material [41] and

*Contact author: p.rani@tue.nl
†Contact author: dominik.juraschek@unifr.ch

Published by the American Physical Society under the terms of the Creative Commons Attribution 4.0 International license. Further distribution of this work must maintain attribution to the author(s) and the published article's title, journal citation, and DOI.

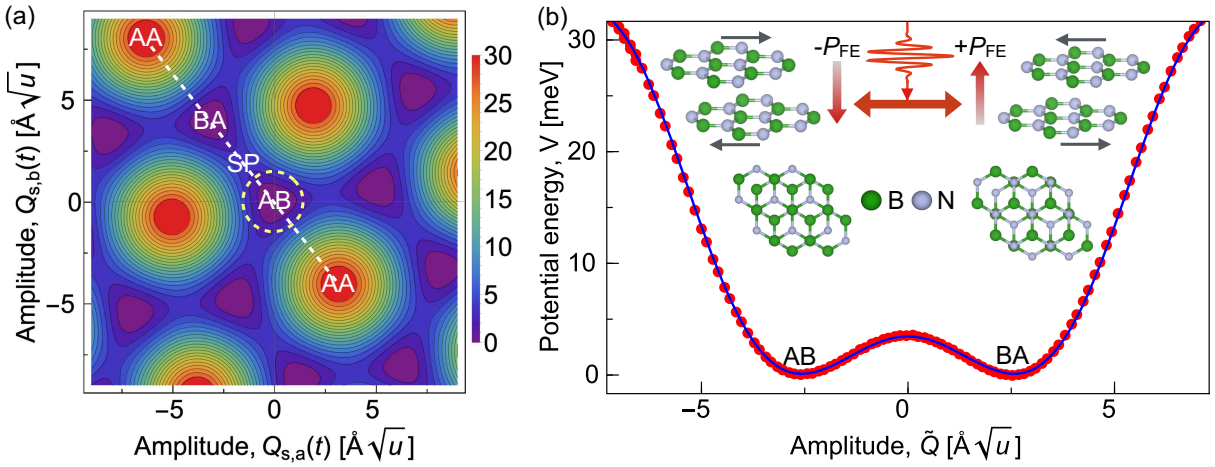


FIG. 1. Phononic sliding in hexagonal boron nitride. (a) Potential energy landscape as a function of shear-mode amplitude. The sixfold rotationally symmetric minima correspond to *AB* and *BA* stacking orders with opposing out-of-plane ferroelectric polarizations, P_{FE}, the local maxima correspond to *AA* stacking (paraelectric phase), and SP is a saddle point with in-plane polarization). The white dashed line corresponds to the double-well potential shown in (b). Double-well potential of the ferroelectric *AB* and *BA* stacking orders. In *AB* stacking, nitrogen atoms from the upper layer are centered over the hexagonal ring, whereas boron atoms from the upper layer are located over nitrogen atoms from the lower layer—vice versa for *BA* stacking. The red dots are calculated data and the blue line is a fit. Gray arrows denote motion of the layers along the shear mode.

references therein [42–48]. We show the calculated potential energy landscape formed by the two orthogonal shear-mode components, $Q_{s,a}$ and $Q_{s,b}$, in Fig. 1(a). The minima correspond to *AB* and *BA* stacking orders with opposing ferroelectric polarizations, illustrated in Fig. 1(b). There, we show the double-well potential corresponding to the dashed linecut in (a).

The goal of this Letter is to find an efficient mechanism that allows us to switch between the two stacking orders by the means of shear-mode excitation. We investigate two key aspects of the shear-mode dynamics: first, we compare the efficiency of different coherent excitation mechanisms for the shear mode while remaining within one stacking order. Second, we demonstrate switching along the pathway represented by the dotted white line in Fig. 1(a) by considering the full double-well potential.

Shear-mode excitation mechanisms—We consider four prominent excitation mechanisms for the shear modes, IRA, IRS, ISRS, and THz SFE in the *AB*-stacked ferroelectric phase (dashed yellow circle) in Fig 1. We do not consider above-band-gap excitation mechanisms such as displacive excitation of coherent phonons (DECP) that would require ultraviolet pulses and lead to additional electronic dissipative effects [28,30,49]. The coherent phonon dynamics can be described by semiclassical equations of motion, for which we compute the parameters from first principles [32,35,36,50],

$$\ddot{\mathbf{Q}}_s + \kappa\dot{\mathbf{Q}}_s + \Omega^2\mathbf{Q}_s + \mathbf{F}(t) = 0. \tag{1}$$

Here, $\mathbf{Q}_s = (Q_{s,a}, Q_{s,b}, 0)$ contains the amplitudes of the two orthogonal components of the shear mode. We set the damping to $\kappa_s = 0.1 \times \Omega_s/(2\pi)$ for the shear mode, in agreement with typical shear-mode dampings found in h-BN [51]. $\mathbf{F}(t) = -\nabla_{\mathbf{Q}} V_{\text{int}}$ is the driving force that is given by the interaction potential V_{int}, containing both light-matter and nonlinear phonon couplings. We model the laser pulse with $\mathbf{E}(t,\phi,\theta) = \tilde{E}_0 \exp[-t^2/(2(\tau/\sqrt{8\ln 2})^2)][\cos(\omega_0 t)\cos(\theta), \cos(\omega_0 t + \phi)\sin(\theta), 0]$, where $\tilde{E}_0 = 2E_0/(1+\sqrt{\epsilon_{2D}})$ is the reduced electric field of the pulse, accounting for electronic screening in the material from the in-plane dielectric function, which we compute to be $\epsilon_{2D} = 4.77$, consistent with literature values [52–54]. τ is the full width at half maximum pulse duration and ω_0 is the center frequency. ϕ and θ control the polarization state and orientation of the pulse and their respective values for the different mechanisms are provided in Supplemental Material [41]. We list E_0, τ, and ω_0 to be used for the four mechanisms in Table I. We chose parameters for a strong, yet experimentally achievable pulse for IRA as a reference and adjust pulse duration and peak electric field for the

TABLE I. Parameters for the comparison of the shear-mode excitation mechanisms. ω_0 is the center frequency, τ the full width at half maximum duration, and E_0 the peak electric field of the laser pulse. The pulse energy $\propto E_0^2\tau$ is constant in all cases. $|\mathbf{Q}_s|$ denotes the maximum shear-mode amplitude. For IRS and ISRS, two pulses are used each.

Mechanisms	IRA	IRS	ISRS	THz SFE
$\omega_0/(2\pi)$(THz)	1	40.5	374	0.5
τ (ps)	1	0.05	0.05	2
E_0(MV/cm)	12.7	40.2	40.2	9
$\lvert\mathbf{Q}_s\rvert$(pm$\sqrt{u}$)	11	8	0.09	0.04

other mechanisms so that the total pulse energy $\propto E_0^2\tau$ remains constant.

The first mechanism we investigate is IRA, which is described by the direct coupling of the electric dipole moment of the phonon mode to the electric field of light, $V_{\mathrm{int}} = Q_{s,a/b}\mathbf{Z}\cdot\mathbf{E}(t)$. Here, $\mathbf{Z} = \sum_\alpha Z_\alpha^* \mathbf{q}_{s,\alpha}/\sqrt{M_\alpha}$ is the mode effective charge vector, where Z^* is the Born effective charge tensor, $\mathbf{q}_{s,\alpha}$ is the phonon eigenvector, and M_α the atomic mass of atom α in the unit cell. The atomic displacements along the phonon eigenvectors of the shear modes are shown in Fig. 2(e). This mechanism requires resonant excitation of the phonon mode, $\omega_0 = \Omega_s$, and corresponds to a one photon absorption process by the phonon, illustrated in Fig. 2(a). In semiconductors and insulators, IRA is generally the most efficient mechanism to induce coherent phonon oscillations with large amplitudes, leading to the field of nonlinear phononics within the past decade [31,32,55]. While in bulk oxides, $|\mathbf{Z}| \sim 1e/\sqrt{u}$ [38,56,57], where e is the elementary charge and u the atomic mass unit, we find the mode effective charge of the shear modes in h-BN to be only $|\mathbf{Z}_s| = 0.002e/\sqrt{u}$. The dynamics according to Eq. (1) yield a maximum phonon amplitude of $|\mathbf{Q}_s| = 11\ \mathrm{pm}\sqrt{u}$, which we show in Fig. 2(a). This weak light-matter coupling explains why giant pulse energies were needed to predict switching of a van der Waals ferroelectric with infrared absorption in a previous study [27].

The second mechanism we investigate is IRS. Because of the lack of inversion symmetry, the shear modes are both infrared and Raman active. In IRS, the laser pulse first excites high-frequency intralayer phonon modes through infrared absorption that then couple to the shear modes through nonlinear phonon interactions [31,32,58]. At the same time, the phonon excitation leads to rectification of the coupled phonon mode, also called phononic rectification, see Fig. 2(b). In bulk ferroelectrics, phononic rectification has been previously used to transiently switch ferroelectricity [1,3,11,12,58]. The interaction potential is given by $V_{\mathrm{int}}(t) = 2c_n Q_{n,x}Q_{n,y}Q_{s,a} + c_n(Q_{n,x}^2 - Q_{n,y}^2)Q_{s,b} + Q_{n,x/y}\mathbf{Z}_n\cdot\mathbf{E}(t)$, where $\mathbf{Q}_n = (Q_{n,x}, Q_{n,y}, 0)$ is the amplitude vector of a high-frequency intralayer mode, n, $\mathbf{Z}_n$ is its mode effective charge vector, and c_n is the nonlinear phonon coupling. The calculated eigenfrequencies of the two high-frequency E modes are $\Omega_1/(2\pi) = 40.45$ THz and $\Omega_2/(2\pi) = 40.5$ THz and the corresponding atomic displacements are shown in Fig. 2(e). We find the mode effective charges to be $|\mathbf{Z}_1| = 1.4e/\sqrt{u}$ and $|\mathbf{Z}_2| = 0.7e/\sqrt{u}$, as well as the nonlinear phonon couplings to be $c_1 = 0.93\ \mathrm{meV}/(\text{Å}\sqrt{u})^3$ and $c_2 = 5.3\ \mathrm{meV}/(\text{Å}\sqrt{u})^3$, respectively. The damping for high-frequency mode we took is $\kappa_n = 0.02\times\Omega_n/(2\pi)$ which is in good agreement with the literature [59–61]. To evaluate the phonon dynamics, Eq. (1) is expanded to include equations of motion for the high-frequency phonon modes, see Supplemental Material for details [41]. In order to achieve circular excitation, two linearly polarized laser pulses have to be applied with a time delay of $\Delta t = 1/(4\Omega_s)$ and a relative angle of $\theta = 45°$. Both pulses are

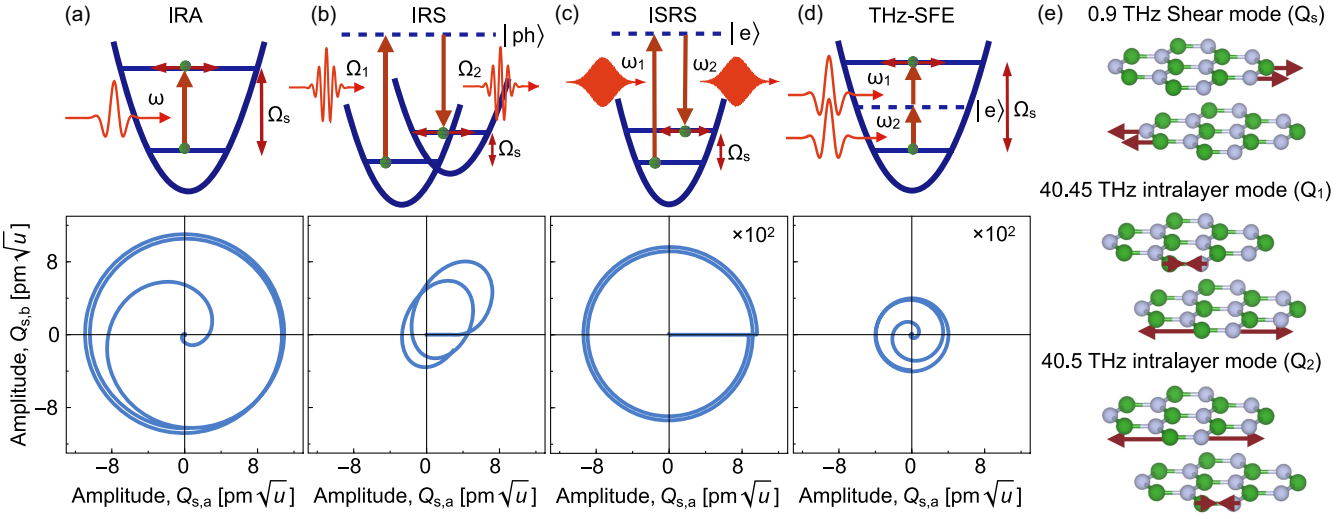


FIG. 2. Shear-mode excitation mechanisms for circular polarization in AB stacking. Energy diagrams (top row) depict the scattering processes, where red pulses indicate incoming and outgoing photons and dashed lines mark intermediate electronic $|\mathrm{e}\rangle$ and phononic $|\mathrm{ph}\rangle$ states in the Raman-type processes. We plot the time evolutions of the amplitudes of the two orthogonal shear-mode components following the excitation for a time window up to 3 ps. (a) Infrared absorption (IRA), (b) ionic Raman scattering (IRS), (c) impulsive stimulated Raman scattering (ISRS), and (d) terahertz sum-frequency excitation (THz SFE). (e) Visualization of eigenvectors of the 0.9 THz interlayer shear mode (Q_s), as well as the 40.45 THz (Q_1) and 40.5 THz (Q_2) intralayer modes in AB stacking. The intralayer modes exhibit similar displacement patterns in terms of direction, however, differing magnitudes of relative displacement in the two layers that interchange between AB and BA stacking.

tuned to resonance with the high-frequency phonon modes, $\omega_0/(2\pi) = 40.5$ THz. We show the dynamics in Fig. 2(b). The shear-mode amplitude generated by IRS reaches $|\mathbf{Q}_s| = 8$ pm$\sqrt{u}$, which is slightly smaller than that arising from infrared absorption. The weak response is a result of the small cubic-order nonlinear phonon couplings. These factors are the reason why giant pulse energies were needed to predict switching of a van der Waals ferroelectric through conventional nonlinear phononics in a previous study [26].

The third and fourth mechanisms we investigate are ISRS and THz SFE, which are described by the same fundamental coupling term. In ISRS, the difference frequency of two photons from the laser pulse is resonant with the shear mode, as illustrated in Fig. 2(c) [33], while in THz SFE, two photons from the ultrashort laser pulse are absorbed by a phonon, as illustrated in Fig. 2(d) [34,35,62–69]. The interaction potential for both mechanisms is given by $V_{\mathrm{int}}(t) = 2R\epsilon_0 E_x E_y Q_{s,a} + R\epsilon_0(E_x^2 - E_y^2)Q_{s,b}$, where R is the single independent component of the Raman tensor. Our calculations yield $R(1.55\ \mathrm{eV}) = 0.09\ \text{Å}^2\sqrt{u}$ and $R(0.47\ \mathrm{eV}) = 0.04\ \text{Å}^2\sqrt{u}$, see Supplemental Material for the full frequency dependence and symmetry [41]. As in IRS, in order to achieve circular excitation for ISRS, two linearly polarized pulses have to be applied with a time delay of $\Delta t = 1/(4\Omega_s)$ and a relative angle of $\theta = 135°$. For THz SFE in turn, a circularly polarized pulse is used. We show the shear-mode dynamics in Figs. 2(c) and 2(d). The maximum amplitude reaches $|\mathbf{Q}_s| = 0.09$ pm$\sqrt{u}$ for ISRS and 0.04 pm$\sqrt{u}$ for THz SFE. The amplitude for both mechanisms are much smaller than those of IRA and IRS, because of the particularly small values of the Raman tensor (three orders of magnitude smaller than that of diamond [35]). We further investigated infrared resonant Raman scattering [70], which we found to yield an even smaller amplitude however, see Supplemental Material [41].

The calculations were performed for circular excitations of the shear modes in order to not be biased toward any particular direction in Fig. 1(a). Full directional control through the phase of the shear modes is illustrated in Fig. S11 in Supplemental Material [41]. Our simulations yield shear-mode amplitudes of up to 11 pm$\sqrt{u}$ for IRA and 8 pm$\sqrt{u}$ for IRS, whereas the other mechanisms yield much smaller amplitudes. It shall be noted that the phonon amplitude generated by IRA scales linearly with the electric field, whereas all Raman-type mechanisms scale quadratically, possibly leading to larger amplitudes as the pulse energy increases. To overcome the energy barrier however, an amplitude of at least 2.58 Å$\sqrt{u}$ is required. We therefore evaluated the critical pulse energies at which the different mechanisms would lead to ferroelectric switching, see Supplemental Material [41]. All four mechanisms require unfeasibly strong pulses, making switching based on conventional coherent excitation impractical. We therefore investigate an alternative approach that efficiently reduces the switching threshold, by explicitly taking into account the time-dependent double-well potential of the shear modes upon strong driving of the high-frequency intralayer modes.

Ferroelectric switching with nonlinear phononic slidetronics—The shear modes are launched along the path indicated in Fig. 1(a), parametrized by the generalized shear-mode coordinate $\tilde{Q}$, to transition between *AB* and *BA* stacking orders. The potential energy of the double well can be written as $\tilde{V} = \alpha\tilde{Q}^2 + \beta\tilde{Q}^4 + \gamma\tilde{Q}^6 + \delta\tilde{Q}^8$. The equation of motion for $\tilde{Q}$ accordingly becomes

$$\ddot{\tilde{Q}} + \kappa\dot{\tilde{Q}} + \frac{\partial\tilde{V}}{\partial\tilde{Q}} = 0. \tag{2}$$

In Fig. 3(a), we show calculations for the tilting of the potential-energy landscape of the shear modes upon displacing the *E* mode at 40.5 THz, Q_2, leading to a dynamical lifting of the degeneracy of the energy minima of *AB* and

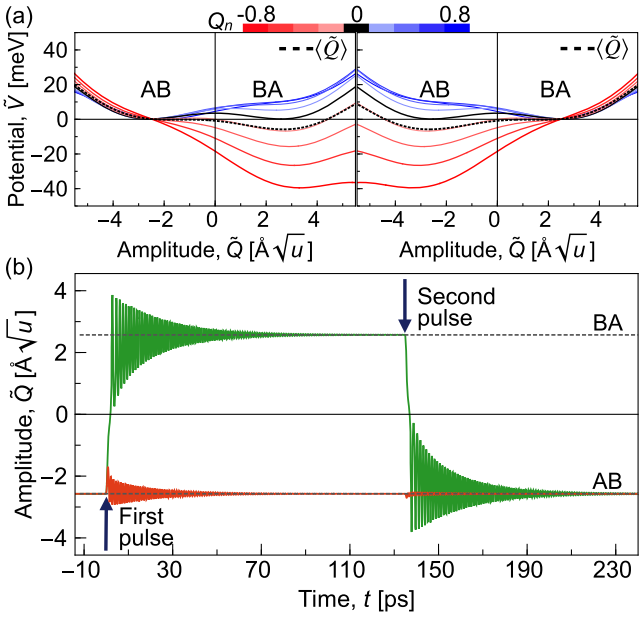


FIG. 3. Ferroelectric switching with nonlinear phononic slidetronics. (a) Tilting of the double-well potential, $\tilde{V}(\tilde{Q})$, when the 40.5 THz intralayer *E* mode, Q_n, is displaced from −0.8 to 0.8 Å$\sqrt{u}$. Left, displacement of Q_n in *AB* stacking, and right, in *BA* stacking. The dotted black curve is the average of $\tilde{V}$ obtained from tiltings due to the positive (blue curves) and negative (red curves) amplitudes of the 40.5 THz mode. (b) Time evolution of shear-mode amplitude, $\tilde{Q}$, following the excitation of the 40.5 THz mode. The red curve shows rectified coherent oscillations of the shear mode in *AB* stacking for a pulse energy below the switching threshold ($E_0 = 17.5$ MV/cm). The green curve shows the shear-mode amplitude overcoming the barrier and switching from *AB* to *BA* stacking after the excitation with a pulse energy above the switching threshold ($E_0 = 20.35$ MV/cm).The second laser pulse after 135 ps switches the system back to *AB* stacking.

BA stacking orders. While the potential will tilt back and forth at high frequency for positive and negative amplitudes of Q_2, the dynamical average $\langle\tilde{Q}\rangle$ shows a net tilting (black dotted curve). The *E* mode at 40.45 THz only leads to weak modulations and is therefore neglected, see Fig. S10 in Supplemental Material [41]. As a result of the tilting, the double-well potential gains contributions with odd powers in $\tilde{Q}$, and we can model the coefficients of $\tilde{V}$ as time-dependent functionals of the 40.5 THz *E*-mode amplitude, $\tilde{V}[Q_2(t)]$, as

$$\tilde{V}[Q_2] = \sum_{m=0}^{8} \sigma^m (a_m + b_m Q_2 + c_m Q_2^2)\tilde{Q}^m, \qquad (3)$$

where $\sigma = \pm 1$ for *AB* and *BA* stacking, respectively. The coefficients are obtained by a least-mean-squares fit of Eq. (3) to the calculated potential-energy surface. For details, see Supplemental Material [41]. Because $\tilde{Q}$ refers to the coordinate of the entire double-well potential, these odd powers go beyond conventional ionic Raman scattering that describes coupling to the shear displacement within the same stacking geometry.

In Fig. 3(b), we show the temporal evolution of the generalized shear-mode coordinate following the excitation. The 40.5 THz mode starts ringing and dynamically tilts the double-well potential. We find the switching threshold to be reached when the 40.5 THz mode is excited using a laser pulse with a peak electric field of $E_0 = 20.35$ MV/cm and a pulse duration of $\tau = 0.5$ ps, which is shorter than the polarization switching time of about 2.5 ps. The orientation of the pulse is described by $\phi = \Delta t = \theta = 0$. These specifications lie well within experimentally achievable pulse strengths [71,72]. The generalized shear-mode coordinate crosses the energy barrier starting from *AB* stacking and then relaxes into the *BA* stacking configuration, reversing the ferroelectric polarization in the process. An excitation in the *BA* stacking configuration with a second pulse reciprocally switches back to *AB* stacking. For an excitation with a pulse energy below the switching threshold, here $E = 17.5$ MV/cm, the shear mode simply gets coherently excited and relaxes back into the original stacking configuration.

Discussion—Our results demonstrate that ferroelectricity in bilayer h-BN can be efficiently switched by tilting the interlayer shear-mode potential through high-frequency intralayer phonon excitation. The pulse strengths required to overcome the energy barrier between stacking orders are readily achievable with state-of-the-art tabletop pump-probe setups and the reversal of ferroelectric polarization can be measured with terahertz pump-second harmonic generation probe measurements. The mechanism we describe is generally applicable to bi- and multilayer van der Waals materials, such as transition metal di- and trichalcogenides (e.g., WTe_2, CrI_3) or transition metal phosphorus trichalcogenides (e.g., $MnPSe_3, VPS_3$), enabling light-induced control of stacking order that can be extended to other electronic orders, including magnetism and topology [22,73–76].

We note that the switching threshold is sensitive to the damping of the shear modes that allows them to deterministically relax into one of the energy minima and therefore stacking configuration. Phonon damping in van der Waals materials can be strongly influenced by sample quality and even isotopic purity [60,61]. For large damping and short phonon lifetimes, the pulse energy to reach the switching threshold increases. In turn, for small damping and long phonon lifetimes, the shear mode can oscillate back and forth between the two stacking orders which requires fine tuning of the pulse strength. We show corresponding simulations in Supplemental Material [41]. We use shear-mode dampings matching those found in experiment [51], however, these strictly only apply to displacements of the shear-mode coordinate around the equilibrium position. Not captured by our model are explicit couplings of the shear modes to the acoustic branches [38,77], which may be modified out of equilibrium and lead to modifications of the damping during the dynamics. A more comprehensive treatment therefore will need to take into account amplitude- and time-dependent damping modulations in the future.

Our results demonstrate nonlinear phononic slidetronics as a viable avenue for changing the stacking order and therefore structural and electronically ordered phases of van der Waals materials. This mechanism could serve as a base for highly efficient all-optically controlled low-dimensional ferroelectric memory devices in the future.

Acknowledgments—We thank E. Baldini, D. Kaplan, L. Benfatto, E. Demler, and O. Yaniv for useful discussions. This work was supported by the Army Research Office Grant No. W911NF-23-1-0243. Calculations were performed on HPC infrastructure at Tel Aviv University.

Data availability—The data that support the findings of this article are openly available in Ref. [78].

[1] A. Subedi, Proposal for ultrafast switching of ferroelectrics using midinfrared pulses, Phys. Rev. B **92**, 214303 (2015).
[2] R. Mankowsky, A. Von Hoegen, M. Först, and A. Cavalleri, Ultrafast reversal of the ferroelectric polarization, Phys. Rev. Lett. **118**, 197601 (2017).
[3] M. Henstridge, M. Först, E. Rowe, M. Fechner, and A. Cavalleri, Nonlocal nonlinear phononics, Nat. Phys. **18**, 457 (2022).
[4] P. Chen, C. Paillard, H. J. Zhao, J. Íñiguez, and L. Bellaiche, Deterministic control of ferroelectric polarization by ultrafast laser pulses, Nat. Commun. **13**, 2566 (2022).

[5] M. Kwaaitaal, D. G. Lourens, C. S. Davies, and A. Kirilyuk, Epsilon-near-zero regime enables permanent ultrafast all-optical reversal of ferroelectric polarization, Nat. Photonics **18**, 569 (2024).
[6] J. Shi, C. Heide, H. Xu, Y. Huang, Y. Shen, B. Guzelturk, M. Henstridge, C. F. Schön, A. Mangu, Y. Kobayashi *et al.*, Nonresonant Raman control of material phases, arXiv:2411.10131.
[7] X. Li, T. Qiu, J. Zhang, E. Baldini, J. Lu, A. M. Rappe, and K. A. Nelson, Terahertz field–induced ferroelectricity in quantum paraelectric $SrTiO_3$, Science **364**, 1079 (2019).
[8] T. Nova, A. Disa, M. Fechner, and A. Cavalleri, Metastable ferroelectricity in optically strained $SrTiO_3$, Science **364**, 1075 (2019).
[9] D. Shin, S. Latini, C. Schäfer, S. A. Sato, E. Baldini, U. De Giovannini, H. Hübener, and A. Rubio, Simulating terahertz field-induced ferroelectricity in quantum paraelectric $SrTiO_3$, Phys. Rev. Lett. **129**, 167401 (2022).
[10] M. Fechner, M. Först, G. Orenstein, V. Krapivin, A. S. Disa, M. Buzzi, A. von Hoegen, G. de la Pena, Q. L. Nguyen, R. Mankowsky, M. Sander, H. Lemke, Y. Deng, M. Trigo, and A. Cavalleri, Quenched lattice fluctuations in optically driven $SrTiO_3$, Nat. Mater. **23**, 363 (2024).
[11] V. A. Abalmasov, Ultrafast reversal of the ferroelectric polarization by a midinfrared pulse, Phys. Rev. B **101**, 014102 (2020).
[12] V. A. Abalmasov, Ferroelectric polarization reversal vs pump spot shape, Phys. Rev. B **104**, L140102 (2021).
[13] J. Wu and M. Li, Sliding ferroelectricity in 2D van der Waals materials: Related physics and future opportunities, Proc. Natl. Acad. Sci. U.S.A. **118**, e2115703118 (2021).
[14] C. Wang, L. You, D. Cobden, and J. Wang, Towards two-dimensional van der Waals ferroelectrics, Nat. Mater. **22**, 542 (2023).
[15] M. Vizner Stern, Y. Waschitz, W. Cao, I. Nevo, K. Watanabe, T. Taniguchi, E. Sela, M. Urbakh, O. Hod, and M. Ben Shalom, Interfacial ferroelectricity by van der Waals sliding, Science **372**, 1462 (2021).
[16] P. Meng, Y. Wu, R. Bian, E. Pan, B. Dong, X. Zhao, J. Chen, L. Wu, Y. Sun, Q. Fu, Q. Liu, D. Shi, Q. Zhang, Y.-W. Zhang, Z. Liu, and F. Liu, Sliding induced multiple polarization states in two-dimensional ferroelectrics, Nat. Commun. **13**, 7696 (2022).
[17] K. Yasuda, E. Zalys-Geller, X. Wang, D. Bennett, S. S. Cheema, K. Watanabe, T. Taniguchi, E. Kaxiras, P. Jarillo-Herrero, and R. Ashoori, Ultrafast high-endurance memory based on sliding ferroelectrics, Science **385**, 53 (2024).
[18] R. Bian, R. He, E. Pan, Z. Li, G. Cao, P. Meng, J. Chen, Q. Liu, Z. Zhong, W. Li, and F. Liu, Developing fatigue-resistant ferroelectrics using interlayer sliding switching, Science **385**, 57 (2024).
[19] M. Vizner Stern, S. Salleh Atri, and M. Ben Shalom, Sliding van der Waals polytypes, Nat. Phys. **7**, 50 (2025).
[20] S. Deng, H. Yu, J. Ji, C. Xu, and H. Xiang, Deterministic and efficient switching of sliding ferroelectrics, Phys. Rev. B **111**, 174105 (2025).
[21] P. Tang and Gerrit E. W. Bauer, Sliding phase transition in ferroelectric van der Waals bilayers, Phys. Rev. Lett. **130**, 176801 (2023).
[22] E. J. Sie *et al.*, An ultrafast symmetry switch in a Weyl semimetal, Nature (London) **565**, 61 (2019).
[23] M. Y. Zhang, Z. X. Wang, Y. N. Li, L. Y. Shi, D. Wu, T. Lin, S. J. Zhang, Y. Q. Liu, Q. M. Liu, J. Wang, T. Dong, and N. L. Wang, Light-induced subpicosecond lattice symmetry switch in $MoTe_2$, Phys. Rev. X **9**, 021036 (2019).
[24] T. Fukuda, K. Makino, Y. Saito, P. Fons, A. V. Kolobov, K. Ueno, and M. Hase, Ultrafast dynamics of the low frequency shear phonon in 1T'-$MoTe_2$, Appl. Phys. Lett. **116**, 093103 (2020).
[25] H. Rostami, Theory for shear displacement by light-induced Raman force in bilayer graphene, Phys. Rev. B **106**, 155405 (2022).
[26] J. Park, I. W. Yeu, G. Han, C. S. Hwang, and J.-H. Choi, Ferroelectric switching in bilayer 3R MoS_2 via interlayer shear mode driven by nonlinear phononics, Sci. Rep. **9**, 14919 (2019).
[27] J. Wang, X. Li, X. Ma, L. Chen, J.-M. Liu, C.-G. Duan, J. Íñiguez-González, D. Wu, and Y. Yang, Ultrafast switching of sliding polarization and dynamical magnetic field in van der Waals bilayers induced by light, Phys. Rev. Lett. **133**, 126801 (2024).
[28] Q. Yang and S. Meng, Light-induced complete reversal of ferroelectric polarization in sliding ferroelectrics, Phys. Rev. Lett. **133**, 136902 (2024).
[29] L. Gao and L. Bellaiche, Large photoinduced tuning of ferroelectricity in sliding ferroelectrics, Phys. Rev. Lett. **133**, 196801 (2024).
[30] H. Wei, D. Kaplan, H. Xu, and J. Li, Ultrafast switchable polar and magnetic orders by nonlinear light-matter interaction, arXiv:2504.04662.
[31] M. Först, C. Manzoni, S. Kaiser, Y. Tomioka, Y. Tokura, R. Merlin, and A. Cavalleri, Nonlinear phononics as an ultrafast route to lattice control, Nat. Phys. **7**, 854 (2011).
[32] A. Subedi, A. Cavalleri, and A. Georges, Theory of nonlinear phononics for coherent light control of solids, Phys. Rev. B **89**, 220301(R) (2014).
[33] R. Merlin, Generating coherent THz phonons with light pulses, Solid State Commun. **102**, 207 (1997).
[34] S. Maehrlein, A. Paarmann, M. Wolf, and T. Kampfrath, Terahertz sum-frequency excitation of a Raman-active phonon, Phys. Rev. Lett. **119**, 127402 (2017).
[35] D. M. Juraschek and S. F. Maehrlein, Sum-frequency ionic Raman scattering, Phys. Rev. B **97**, 174302 (2018).
[36] M. Fechner and N. A. Spaldin, Effects of intense optical phonon pumping on the structure and electronic properties of yttrium barium copper oxide, Phys. Rev. B **94**, 134307 (2016).
[37] D. M. Juraschek, M. Fechner, and N. A. Spaldin, Ultrafast structure switching through nonlinear phononics, Phys. Rev. Lett. **118**, 054101 (2017).
[38] G. Khalsa, J. Z. Kaaret, and N. A. Benedek, Coherent control of the translational and point group symmetries of crystals with light, Phys. Rev. B **109**, 024110 (2024).
[39] D. Wickramaratne, L. Weston, and C. G. Van de Walle, Monolayer to bulk properties of hexagonal boron nitride, J. Phys. Chem. C **122**, 25524 (2018).
[40] H. Ma, C. Yang, B. Ni, Y. Li, S. Huang, W. Lin, and Y. Zhang, Artificial stacking dependences of band structures

and second-harmonic generations in bilayer hexagonal boron nitride, ACS Nano **19**, 16569 (2025).
[41] See Supplemental Material at http://link.aps.org/supplemental/10.1103/5kfl-11m1 for computational details, list of phonon modes, laser-pulse specifications, Raman-tensor calculations, high-frequency intralayer phonon mode amplitudes, ferroelectric switching achieved from different mechanisms, potential energy fitting parameters, time-dependent double-well potential, tilting of the double-well potential upon displacement of Q1, and comparison of pulse fluences, angle-dependent mode effective charge for shear mode, phase control of the shear modes.
[42] G. Kresse and J. Furthmüller, Efficiency of ab-initio total energy calculations for metals and semiconductors using a plane-wave basis set, Comput. Mater. Sci. **6**, 15 (1996).
[43] G. Kresse and J. Furthmüller, Efficient iterative schemes for ab initio total-energy calculations using a plane-wave basis set, Phys. Rev. B **54**, 11169 (1996).
[44] A. Togo and I. Tanaka, First principles phonon calculations in materials science, Scr. Mater. **108**, 1 (2015).
[45] G. I. Csonka, J. P. Perdew, A. Ruzsinszky, P. H. Philipsen, S. Lebègue, J. Paier, O. A. Vydrov, and J. G. Ángyán, Assessing the performance of recent density functionals for bulk solids, Phys. Rev. B **79**, 155107 (2009).
[46] H. J. Monkhorst and J. D. Pack, Special points for Brillouin-zone integrations, Phys. Rev. B **13**, 5188 (1976).
[47] G. Constantinescu, A. Kuc, and T. Heine, Stacking in bulk and bilayer hexagonal boron nitride, Phys. Rev. Lett. **111**, 036104 (2013).
[48] A. V. Lebedev, I. V. Lebedeva, A. A. Knizhnik, and A. M. Popov, Interlayer interaction and related properties of bilayer hexagonal boron nitride: *Ab initio* study, RSC Adv. **6**, 6423 (2016).
[49] D. O. Horiachyi, M. O. Nestoklon, I. A. Akimov, A. V. Trifonov, N. V. Siverin, N. E. Kopteva, A. N. Kosarev, D. R. Yakovlev, V. E. Gusev, M. Fries *et al.*, Efficient launching of shear phonons in photostrictive halide perovskites, Sci. Adv. **11**, eadw9172 (2025).
[50] A. von Hoegen, R. Mankowsky, M. Fechner, M. Först, and A. Cavalleri, Probing the interatomic potential of solids with strong-field nonlinear phononics, Nature (London) **555**, 79 (2018).
[51] T. Kang, J. Zhang, A. Kundu, K. Reimann, M. Woerner, T. Elsaesser, B. Gil, G. Cassabois, C. Flytzanis, G. Fugallo *et al.*, Ultrafast nonlinear phonon response of few-layer hexagonal boron nitride, Phys. Rev. B **104**, L140302 (2021).
[52] S. M. Gilbert, T. Pham, M. Dogan, S. Oh, B. Shevitski, G. Schumm, S. Liu, P. Ercius, S. Aloni, M. L. Cohen *et al.*, Alternative stacking sequences in hexagonal boron nitride, 2D Mater. **6**, 021006 (2019).
[53] A. Laturia, M. L. Van de Put, and W. G. Vandenberghe, Dielectric properties of hexagonal boron nitride and transition metal dichalcogenides: From monolayer to bulk, npj 2D Mater. Appl. **2**, 6 (2018).
[54] N. Ohba, K. Miwa, N. Nagasako, and A. Fukumoto, First-principles study on structural, dielectric, and dynamical properties for three BN polytypes, Phys. Rev. B **63**, 115207 (2001).
[55] A. S. Disa, T. F. Nova, and A. Cavalleri, Engineering crystal structures with light, Nat. Phys. **17**, 1087 (2021).
[56] D. M. Juraschek and N. A. Spaldin, Orbital magnetic moments of phonons, Phys. Rev. Mater. **3**, 064405 (2019).
[57] A. Gomez Pueyo and A. Subedi, Light-induced translation symmetry breaking via nonlinear phononics, Phys. Rev. B **106**, 214305 (2022).
[58] R. Mankowsky, M. Först, and A. Cavalleri, Non-equilibrium control of complex solids by nonlinear phononics, Rep. Prog. Phys. **79**, 064503 (2016).
[59] D. M. Juraschek and P. Narang, Highly confined phonon polaritons in monolayers of perovskite oxides, Nano Lett. **21**, 5098 (2021).
[60] A. J. Giles, S. Dai, I. Vurgaftman, T. Hoffman, S. Liu, L. Lindsay, C. T. Ellis, N. Assefa, I. Chatzakis, T. L. Reinecke *et al.*, Ultralow-loss polaritons in isotopically pure boron nitride, Nat. Mater. **17**, 134 (2018).
[61] R. Cuscó, L. Artús, J. H. Edgar, S. Liu, G. Cassabois, and B. Gil, Isotopic effects on phonon anharmonicity in layered van der Waals crystals: Isotopically pure hexagonal boron nitride, Phys. Rev. B **97**, 155435 (2018).
[62] A. A. Melnikov, K. N. Boldyrev, Y. G. Selivanov, V. P. Martovitskii, S. V. Chekalin, and E. A. Ryabov, Coherent phonons in a Bi_2Se_3 film generated by an intense single-cycle THz pulse, Phys. Rev. B **97**, 214304 (2018).
[63] B. E. Knighton, R. T. Hardy, C. L. Johnson, L. M. Rawlings, J. T. Woolley, C. Calderon, A. Urrea, and J. A. Johnson, Terahertz waveform considerations for nonlinearly driving lattice vibrations, J. Appl. Phys. **125**, 144101 (2019).
[64] C. L. Johnson, B. E. Knighton, and J. A. Johnson, Distinguishing nonlinear terahertz excitation pathways with two-dimensional spectroscopy, Phys. Rev. Lett. **122**, 073901 (2019).
[65] A. A. Melnikov, Y. G. Selivanov, and S. V. Chekalin, Phonon-driven ultrafast symmetry lowering in a Bi_2Se_3 crystal, Phys. Rev. B **102**, 224301 (2020).
[66] T. G. H. Blank, K. A. Grishunin, K. A. Zvezdin, N. T. Hai, J. C. Wu, S.-H. Su, J.-C. A. Huang, A. K. Zvezdin, and A. V. Kimel, Two-dimensional terahertz spectroscopy of nonlinear phononics in the topological insulator $MnBi_2Te_4$, Phys. Rev. Lett. **131**, 026902 (2023).
[67] S. Kusaba, H.-W. Lin, R. Tamaki, I. Katayama, J. Takeda, and G. A. Blake, Terahertz sum-frequency excitation of coherent optical phonons in the two-dimensional semiconductor WSe_2, Appl. Phys. Lett. **124**, 122204 (2024).
[68] A. Levchuk, R. Busselez, G. Vaudel, P. Ruello, V. Juvé, and B. Arnaud, Nonlinear phononics in Bi_2Te_3 from first-principles, Phys. Rev. B **112**, 064308 (2025).
[69] O. Minakova, C. Paiva, M. Frenzel, M. S. Spencer, J. M. Urban, C. Ringkamp, M. Wolf, G. Mussler, D. M. Juraschek, and S. F. Maehrlein, Direct observation of angular momentum transfer among crystal lattice modes, Nat. Phys. **22**, 1100 (2026).
[70] G. Khalsa, N. A. Benedek, and J. Moses, Ultrafast control of material optical properties via the infrared resonant Raman effect, Phys. Rev. X **11**, 021067 (2021).
[71] H. Liu, Y. Li, Y. S. You, S. Ghimire, T. F. Heinz, and D. A. Reis, High-harmonic generation from an atomically thin semiconductor, Nat. Phys. **13**, 262 (2017).

[72] C. Vicario, A. Trisorio, S. Allenspach, C. Rüegg, and F. Giorgianni, Narrow-band and tunable intense terahertz pulses for mode-selective coherent phonon excitation, Appl. Phys. Lett. **117**, 101101 (2020).

[73] M. Rodriguez-Vega, Z.-X. Lin, A. Leonardo, A. Ernst, G. Chaudhary, M. G. Vergniory, and G. A. Fiete, Phonon-mediated dimensional crossover in bilayer CrI_3, Phys. Rev. B **102**, 081117(R) (2020).

[74] M. Rodriguez-Vega, M. Vogl, and G. A. Fiete, Direct driving of electronic and phononic degrees of freedom in a honeycomb bilayer with infrared light, Phys. Rev. B **104**, 245135 (2021).

[75] Z.-X. Lin, B. Ma, W. Roberts, M. Rodriguez-Vega, and G. A. Fiete, Interlayer Dzyaloshinskii-Moriya interactions induced via nonlinear phononics in bilayer van der Waals materials, Phys. Rev. B **111**, 115102 (2025).

[76] H. Mavani, K. Huang, K. Samanta, and E. Y. Tsymbal, Two-dimensional antiferromagnets with nonrelativistic spin splitting switchable by electric polarization, Phys. Rev. B **112**, L060401 (2025).

[77] S. W. Teitelbaum, T. Henighan, Y. Huang, H. Liu, M. P. Jiang, D. Zhu, M. Chollet, T. Sato, É. D. Murray, S. Fahy *et al.*, Direct measurement of anharmonic decay channels of a coherent phonon, Phys. Rev. Lett. **121**, 125901 (2018).

[78] P. Rani and D. M. Juraschek, Original code available at Zenodo, 10.5281/zenodo.23079646 (2026).